

Ultrasound imaging to monitor photothermal therapy – Feasibility study

Jignesh Shah^{1,2}, Salavat R. Aglyamov¹, Konstantin Sokolov^{1,2},
Thomas E. Milner¹, Stanislav Y. Emelianov¹

¹Department of Biomedical Engineering, University of Texas at Austin, Austin, TX 78712 USA

²Department of Biomedical Engineering, MD Anderson Cancer Center, Houston, TX 77030 USA

Abstract: This study investigates the feasibility of ultrasound imaging to monitor temperature changes during photothermal treatment. Experiments were performed on tissue-mimicking phantoms and ex-vivo animal tissue samples. Gold nanoparticles were utilized as photoabsorbers. Prior to laser irradiation, structural features of the phantoms and tissue were visualized by ultrasound imaging. Ultrasound thermal imaging, performed during laser heating, showed that the temperature elevation was localized to the region of embedded or injected nanoparticles. The results of our study suggest that ultrasound imaging is a candidate approach to remotely guide photothermal therapy.

©2008 Optical Society of America

OCIS codes: (170.7170) Ultrasound; (350.5340) Photothermal effects; (140.3330) Laser damage; (280.6780) Temperature; (170.1020) Ablation of tissue.

References and links

1. S. N. Goldberg, G. S. Gazelle, and P. R. Mueller, "Thermal ablation therapy for focal malignancy: A unified approach to underlying principles, techniques, and diagnostic imaging guidance," *Am. J. Roentgenol.* **174**, 323-331 (2000).
2. W. R. Chen, R. L. Adams, S. Heaton, D. T. Dickey, K. E. Bartels, and R. E. Nordquist, "Chromophore-enhanced laser-tumor tissue photothermal interaction using an 808-nm diode laser," *Cancer Letters* **88**, 15-19 (1995).
3. L. R. Hirsch, R. J. Stafford, J. A. Bankson, S. R. Sershen, B. Rivera, R. E. Price, J. D. Hazle, N. J. Halas, and J. L. West, "Nanoshell-mediated near-infrared thermal therapy of tumors under magnetic resonance guidance," *Proceedings of the National Academy of Sciences of the United States of America* **100**, 13549-13554 (2003).
4. X. Huang, I. H. El-Sayed, W. Qian, and M. A. El-Sayed, "Cancer cell imaging and photothermal therapy in the near-infrared region by using gold nanorods," *J. Am. Chem. Soc.* **128**, 2115-2120 (2006).
5. Y. Lu, G. L. Liu, J. Kim, Y. X. Mejia, and L. P. Lee, "Nanophotonic crescent moon structures with sharp edge for ultrasensitive biomolecular detection by local electromagnetic field enhancement effect," *Nano. Lett.* **5**, 119-124 (2005).
6. S. K. Hobbs, W. L. Monsky, F. Yuan, W. G. Roberts, L. Griffith, V. P. Torchilin, and R. K. Jain, "Regulation of transport pathways in tumor vessels: role of tumor type and microenvironment," *Proceedings of the National Academy of Sciences of the United States of America* **95**, 4607-4612 (1998).
7. K. Sokolov, M. Follen, J. Aaron, I. Pavlova, A. Malpica, R. Lotan, and R. Richards-Kortum, "Real-time vital optical imaging of precancer using anti-epidermal growth factor receptor antibodies conjugated to gold nanoparticles," *Cancer Res.* **63**, 1999-2004 (2003).
8. W. Teh, and A. R. M. Wilson, "The role of ultrasound in breast cancer screening. A consensus statement by the European Group for breast cancer screening," *European Journal of Cancer* **34**, 449-450 (1998).
9. B. Y. Karlan, and L. D. Platt, "Ovarian cancer screening. The role of ultrasound in early detection.," *Cancer* **76**, 2011-2015 (1995).
10. R. Seip and E. S. Ebbini, "Non-invasive monitoring of ultrasound phased array hyperthermia and surgery treatments," *Engineering in Medicine and Biology Society* **1**, 663-664 (1995).
11. T. Varghese, J. A. Zagzebski, Q. Chen, U. Techavipoo, G. Frank, C. Johnson, A. Wright, and F. T. Lee, Jr., "Ultrasound monitoring of temperature change during radiofrequency ablation: preliminary in-vivo results," *Ultrasound Med. Bio.* **28**, 321-329 (2002).
12. R. Seip, P. VanBaren, C. Simon, and E. S. Ebbini, "Non-invasive spatio-temporal temperature estimation using diagnostic ultrasound," *IEEE Ultrasonics Symposium* **2**, 1613-1616 (1995).
13. J. Shah, S. R. Aglyamov, K. Sokolov, T. E. Milner, and S. Y. Emelianov, "Ultrasound-based thermal and elasticity imaging to assist photothermal cancer therapy - Preliminary study," *IEEE Ultrasonics Symposium*, 1029-1032 (2006).

14. R. Maass-Moreno and C. A. Damianou, "Noninvasive temperature estimation in tissue via ultrasound echo-shifts. Part I. Analytical model," *J. Acoust. Soc. Am.* **100**, 2514-2521 (1996).
15. R. Maass-Moreno, C. A. Damianou, and N. T. Sanghvi, "Noninvasive temperature estimation in tissue via ultrasound echo-shifts. Part II. In vitro study," *J. Acoust. Soc. Am.* **100**, 2522-2530 (1996).
16. J. Ophir, S. K. Alam, B. Garra, F. Kallel, E. Konofagou, T. Krouskop, and T. Varghese, "Elastography: ultrasonic estimation and imaging of the elastic properties of tissues," *Proc Inst Mech Eng* **213**, 203-233 (1999).
17. M. A. Lubinski, S. Y. Emelianov, and M. O'Donnell, "Speckle tracking methods for ultrasonic elasticity imaging using short-time correlation," *IEEE Transactions on Ultrasonics, Ferroelectrics and Frequency Control* **46**, 82-96 (1999).
18. A. Kharine, S. Manohar, R. Seeton, R. G. Kolkman, R. A. Bolt, W. Steenbergen, and F. F. d. Mul, "Poly(vinyl alcohol) gels for use as tissue phantoms in photoacoustic mammography," *Phys. Med. Bio.* **48**, 357-370 (2003).
19. C. M. Hassan and N. A. Peppas, "Structure and applications of poly(vinyl alcohol) hydrogels produced by conventional crosslinking or by freezing/thawing methods," *Advances in polymer science* **153**, 37-65 (2000).
20. G. Frens, "Controlled nucleation for the regulation of the particle size in monodisperse gold suspensions," *Nature Physical Science* **241**, 20-22 (1973).
21. J. C. Bamber and C. R. Hill, "Ultrasonic attenuation and propagation speed in mammalian tissues as a function of temperature," *Ultrasound Med. Bio.* **5**, 149-157 (1979).
22. S. Srinivasan, R. Righetti, and J. Ophir, "Trade-offs between the axial resolution and the signal-to-noise ratio in elastography," *Ultrasound Med. Bio.* **29**, 847-866 (2003).
23. R. Weissleder, "A clearer vision for in vivo imaging," *Nature Biotechnology* **19**, 316-317 (2001).
24. S. Park, S. Mallidi, A. B. Karpiouk, S. Aglyamov, and S. Y. Emelianov, "Photoacoustic Imaging Using Array Transducer," *Proc. SPIE* **6437**, 643714 (2007).
25. A. A. Oraevsky, A. A. Karabutov, S. V. Solomatin, E. V. Savateeva, V. A. Andreev, Z. Gatalica, H. Singh, and R. D. Fleming, "Laser optoacoustic imaging of breast cancer in vivo," *Proc. SPIE* **4256**, 6-15 (2001).
26. R. J. Zemp, R. Bitton, M.-L. Li, K. K. Shung, G. Stoica, and L. V. Wang, "Photoacoustic imaging of the microvasculature with a high-frequency ultrasound array transducer," *J. Biomed. Opt.* **12**, 010501 (2007).
27. S. Thomsen, "Pathologic analysis of photothermal and photomechanical effects of laser-tissue interactions," *Photochem. Photobiol.* **53**, 825-835 (1991).
28. C. Simon, P. D. VanBaren, and E. S. Ebbini, "Motion compensation algorithm for noninvasive two-dimensional temperature estimation using diagnostic pulse-echo ultrasound," *SPIE- Surgical Applications of Energy* **3249**, 182-192 (1998).
29. S. Y. Emelianov, S. R. Aglyamov, A. B. Karpiouk, S. Mallidi, S. Park, S. Sethuraman, J. Shah, R. W. Smalling, J. M. Rubin, and W. G. Scott, "Synergy and applications of combined ultrasound, elasticity, and photoacoustic imaging," *IEEE Ultrasonics Symposium*, 405-415 (2006).
30. A. A. Oraevsky, V. A. Andreev, A. A. Karabutov, D. R. Fleming, Z. Gatalica, H. Singh, and R. O. Esenaliev, "Laser optoacoustic imaging of the breast: detection of cancer angiogenesis," *Proc. SPIE* **3597**, 352-363 (1999).
31. Y. Wang, X. Xie, X. Wang, G. Ku, K. L. Gill, D. P. O'Neal, G. Stoica, and L. V. Wang, "Photoacoustic tomography of a nanoshell contrast agent in the in vivo rat brain," *Nano Lett.* **4**, 1689-1692 (2004).
32. T. Varghese, J. A. Zagzebski, and F. T. Lee, Jr., "Elastographic imaging of thermal lesions in the liver in vivo following radiofrequency ablation: preliminary results," *Ultrasound Med. Bio.* **28**, 1467-1473 (2002).

1. Introduction

Thermal treatments are an alternative to surgery for small, poorly defined lesions and tumors embedded within vital organs [1]. Photothermal therapy relies on the principle of converting radiant energy into heat leading to tumor necrosis. Simple photothermal therapy performed without exogenous photoabsorbers will not discriminate between cancer cells and surrounding tissue. In addition, high laser fluence will be needed to sufficiently heat large or deeply embedded tumors. However, by using near infrared light coupled with photoabsorbers implanted in the tumor, efficient localized heating can be achieved [2-4]. Temperature increases up to 40°C were produced in nanoparticle enhanced photothermal therapy studies causing irreversible tumor damage [2-4]. A variety of metal nanoparticles including gold nanocolloids, nanorods or nanoshells can be used as photoabsorbers [3-5]. Photoabsorbers smaller than 200 nm have been shown to accumulate in a tumor due to a passive mechanism known as enhanced permeability and retention effect [6]. Furthermore, the photoabsorbers can be bioconjugated with anti-bodies to make them tumor specific [7].

However, for good spatial specificity the tumor must first be imaged to identify the size and location of the lesion. In addition, for effective laser dosimetry the temperature increase must be remotely monitored, both spatially and temporally, during the procedure to ensure

tumor necrosis and to protect the surrounding healthy tissue. Finally, the tumor response to therapy must be examined to confirm cancer destruction and to identify possible resurgence. Thus, a need exists for an imaging technique to plan, guide and monitor photothermal therapy. We present a preliminary investigation to utilize ultrasound imaging to identify the therapy site and to monitor the temperature increase.

Ultrasound has been extensively used to image and identify cancerous tissue [8, 9]. Recently ultrasound has been investigated to guide thermal cancer therapies including high intensity focused ultrasound [10] and radiofrequency ablation [11] by monitoring temperature. Apart from ultrasound, thermal imaging during therapy can be performed by various methods including magnetic resonance imaging (MRI), microwave radiometry and impedance tomography. However, compared to other methods, ultrasound has several advantages – being relatively inexpensive, noninvasive and capable of providing instantaneous feedback.

This study reports on the feasibility of ultrasound image guidance of nanoparticle-enhanced photothermal therapy. A laboratory prototype consisting of an ultrasound imaging system interfaced with a continuous wave laser was assembled to perform ultrasound-based thermal imaging during laser irradiation. Gold nanocolloids were utilized as photoabsorbers to efficiently transfer electromagnetic energy into heat within a localized region. Results from tissue/tumor mimicking phantoms and ex-vivo tissue samples demonstrate the ability of ultrasound to identify the tissue abnormalities and monitor the temperature change during laser irradiation. The role of ultrasound imaging to guide photothermal therapy is discussed.

2. Theory

Ultrasound thermal imaging is performed by estimating the apparent time shifts in the ultrasound radiofrequency (RF) signals [11-13]. Figure 1 outlines the procedural steps to estimate the local temperature from the temperature-induced changes in ultrasound signal. The time of echo for ultrasound in a homogenous medium is given by

$$t(T_0) = \frac{2 \cdot z}{c(T_0)}, \quad (1)$$

where $t(T_0)$ is the time delay of the ultrasound echo from scatterer at position z and $c(T_0)$ is the speed of sound in the medium at initial temperature T_0 .

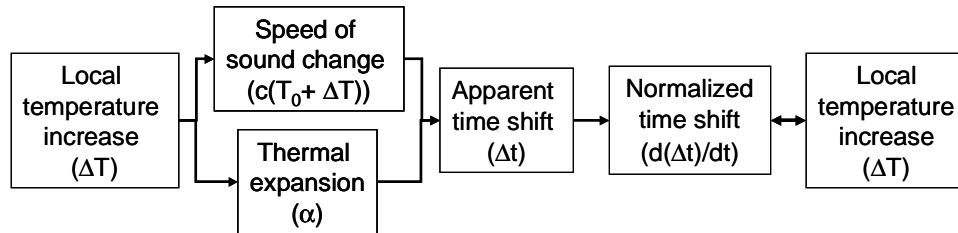


Fig. 1. Block diagram illustrating the principles of ultrasound measurements for thermal imaging.

If the temperature of the medium rises by ΔT , then there is a depth-dependent apparent time shift in the ultrasound signal due to the combined effects of speed of sound changing with temperature and thermal expansion (Fig. 1). The time of echo can now be written as

$$t(T_0 + \Delta T) = \frac{2 \cdot z(1 + \alpha \cdot \Delta T)}{c(T_0 + \Delta T)}, \quad (2)$$

where α is the linear thermal expansion coefficient and $c(T_0 + \Delta T)$ is the speed of sound after temperature elevation. The temperature-induced time shift Δt in ultrasound RF signals

is primarily dependent on the speed of sound change while the effects of thermal expansion can be considered negligible for temperatures below 60°C [14, 15]. Therefore, the time shift can be expressed as

$$\Delta t = t(T_0 + \Delta T) - t(T_0) = 2 \cdot z \cdot \left[\frac{1}{c(T_0 + \Delta T)} - \frac{1}{c(T_0)} \right]. \quad (3)$$

The apparent time shift depends on the speed of sound change and depth/time (since time and distance are equivalent). Therefore for the same temperature rise, ultrasound RF signals received from deeper structures will have greater time shifts. The spatial dependence of the apparent time shift can be removed by differentiating along the axial direction. Therefore, by measuring the time shift in ultrasound, the temperature change can be estimated using the following relationship

$$\Delta T = k \cdot \frac{d(\Delta t)}{dt}, \quad (4)$$

where k is a material dependent property that can be experimentally determined and $d(\Delta t)/dt$, referred to as the normalized time shift, is the spatial gradient of the apparent time shift [11, 12].

Equation (4) can be used to describe both the uniform temperature increase in an homogeneous sample as well as a local and/or spatially varying temperature change ($\Delta T(z)$). To estimate the spatial temperature map during laser heating, multiple ultrasound frames are first acquired during the procedure. Then, the apparent time shift profiles ($\Delta t(z)$) are calculated between successive frames. Finally, the normalized time shift profiles ($d(\Delta t(z))/dt$) are computed by spatially differentiating the apparent time shifts along the direction of ultrasound propagation (z). The normalized time shift can now be directly correlated to the local temperature elevation (Fig. 1).

The normalized apparent time shift ($d(\Delta t(z))/dt$) in Eq. (4) can also be viewed as an apparent temperature-induced strain (not to be confused with a true mechanical strain due to thermal expansion of tissue – such strain is very small and could be ignored for small temperature elevations). To estimate apparent strain and, therefore, temperature, strain estimation techniques routinely used in ultrasound-based elasticity imaging can be used [16]. Indeed, the apparent time shift (or, generally, the displacement) between successive frames can be calculated by using time-delay estimation techniques or motion tracking block matching algorithms similar to those adapted in elasticity imaging [17]. Overall, the normalized time shifts and axial strain are equivalent since both are obtained from the gradient changes in either time shifts or displacements.

3. Materials and methods

3.1. Sample preparation

Experiments were first performed using 50 mm by 50 mm by 50 mm tissue/tumor mimicking phantoms constructed from polyvinyl alcohol (PVA). PVA has modest optical absorption, scatters light similarly to tissue and has been used in constructing tissue phantoms for optical imaging studies [18]. To fabricate the phantoms, 8% by weight aqueous solution of PVA (Sigma-Aldrich, USA) was poured into a mold and set to a desired shape by applying two freeze and thaw cycles of 12 hours each [19]. Silica particles (Sigma-Aldrich, USA) of 40- μ m diameter were added to the phantom body (0.75% by weight) to backscatter the ultrasound. During the phantom preparation, a cylindrical 7-mm diameter inclusion was embedded within the background material to mimic the tumor. The inclusion had a greater concentration of silica particles (1.5% by weight) compared to the surrounding phantom body to produce

acoustic contrast between the inclusion and the background material. In addition, photoabsorbers were embedded in the inclusion. Gold nanocolloids containing 70 nm diameter nanoparticles were used as photoabsorbers. The gold nanocolloids were synthesized by reducing chloroauric acid with sodium citrate [20]. The extinction maximum of the nanocolloids, measured by US-Vis spectroscopy, was close to 532 nm. Laser irradiance of 1 W/cm^2 was applied from the surface of the phantom for 180 seconds.

Ex-vivo studies were performed using fresh porcine longissimus muscle. The samples, sized 30 mm by 30 mm by 15 mm, were immersed in water for acoustic coupling between the ultrasound transducer and tissue. Under ultrasound image guidance, the $20 \mu\text{l}$ solution of gold nanocolloids ($0.5 \cdot 10^{11}$ particles/ml) was slowly injected using a 23-gauge hypodermic needle inserted at an 8 mm depth from the surface of the tissue sample. The needle was inserted such that it was orthogonal to both ultrasound transducer (i.e., ultrasound imaging plane) and laser beam. The injection lasted about 12 seconds while the needle was manually held in the same position. Laser irradiation began immediately after the injection and lasted for 20 seconds. Temperature rise in response to laser power density of 2, 3 and 4 W/cm^2 was estimated by ultrasound imaging.

Additionally to evaluate non-specific temperature increase, a control tissue sample was injected with $20 \mu\text{l}$ of water and was irradiated at 2 W/cm^2 for 120 seconds. The temperature increase obtained was compared with a separate tissue specimen injected with nanoparticles and irradiated with the same laser parameters.

3.2. Experimental setup

The experimental setup for ultrasound guided laser heating (Fig. 2) utilized a frequency-doubled continuous wave Nd:YAG laser with power of up to 4 W. In our experiments, the beam cross-section did not exceed 1 cm diameter. The operating wavelength of the laser, 532-nm, was matched with the photoabsorber's optical resonance. Ultrasound imaging was performed using Sonix RP imaging system (Ultrasonix Medical Corporation, Burnaby, Canada) equipped with 128 element linear array transducer operating at a 5 MHz center frequency. The RF signals were captured at 40 MHz sampling frequency. The experiments were performed at a room temperature of 24°C . A baseline ultrasound frame was captured prior to laser irradiation. During the laser heating procedure, ultrasound frames were acquired every 5 seconds.

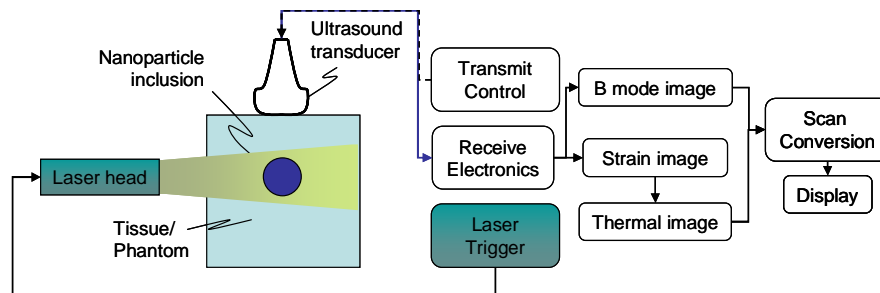


Fig. 2. Experimental setup for ultrasound and thermal imaging during laser heating of the specimen.

3.3. Direct measurements of temperature

Prior to noninvasive thermal imaging, the temperature response of both the tissue mimicking phantom and porcine muscle tissue was determined using a temperature controlled water bath experiment. The sample was placed in a water bath. A thermistor was inserted in the center of the sample to measure temperature. Initially, a baseline ultrasound frame was captured. The temperature of the water bath was then gradually increased from 24°C to 35°C and ultrasound frames were captured for every 1°C temperature increment.

Temperature distribution in the sample was assumed to be spatially homogenous at steady state. Normalized time shifts in the ultrasound signal due to temperature increase were computed in a 10 mm by 10 mm homogenous region near the thermistor. Thus, a normalized time shift versus temperature dependence was obtained for the PVA phantom and porcine muscle tissue (Figs. 3(a) and 3(b)) and approximated using a second-order polynomial fit. Later, the coefficients of the polynomial fit were utilized for remote measurements of temperature by relating the measured normalized time shifts to corresponding temperature during laser heating experiments.

In the temperature range up to 55°C, the normalized time shift in ultrasound signals is primarily caused by the speed of sound changing with temperature since thermal expansion of tissue is small and can be ignored. The speed of sound linearly increases for water and water based tissues between 10–55°C [21]. Therefore, the calibration curves obtained at 24–35°C are also valid at physiological temperature of 37°C. In addition, the temperature elevations of up to 20°C can be measured with the generated curves presented in Fig. 3.

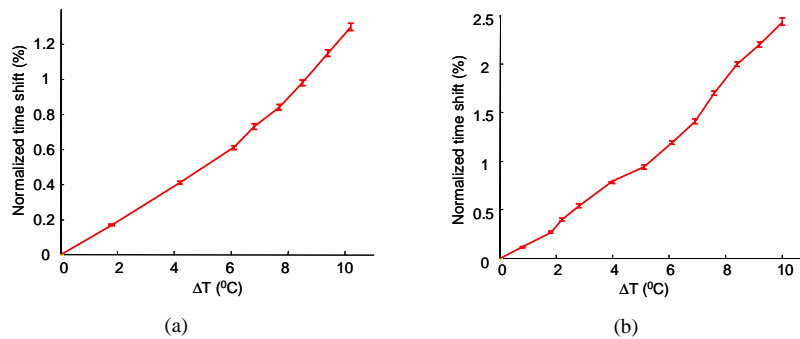


Fig. 3. Temperature calibration for (a) PVA phantom and (b) porcine muscle tissue. The error bars represent standard deviation obtained from 10 measurements.

3.4. Remote measurements of temperature using ultrasound

To compute a thermal image during laser heating, the multiple ultrasound frames were captured during the procedure and stored offline. First, a correlation-based motion tracking algorithm was applied on successive ultrasound frames to estimate the apparent time shifts (or displacements) [17]. A 0.6-mm axial and 2.1-mm lateral kernel was utilized in the motion tracking algorithm. The kernel size was selected given on the trade off between signal-to-noise ratio (SNR) and spatial resolution. A larger kernel size leads to higher SNR while a smaller kernel is needed for better spatial resolution [22]. Interpolation and phase zero-crossings were used to find sub-pixel lateral and axial displacements. Then, the apparent time shifts were differentiated along the axial direction using a 1.6 mm finite difference operator to obtain the normalized time shifts (or strain). Finally, the normalized time shifts were converted to temperature maps by utilizing the relationship obtained from calibration experiments (Fig. 3) for the PVA phantom and porcine muscle tissue.

4. Results

4.1. Phantoms studies

The ultrasound image of tissue mimicking phantom is presented in Fig. 4(a). The thermal images of the phantom recorded during 30, 60 and 180 seconds of laser irradiation are shown in Figs. 4(b-d). All images in Fig. 4 correspond to a 20 mm by 20 mm field of view.

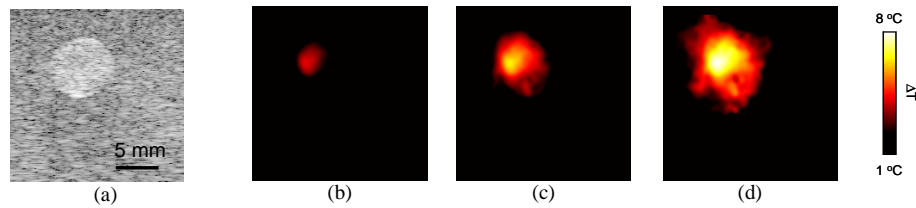


Fig. 4. (a) Ultrasound image of the hyperechoic inclusion with embedded photoabsorbers. (b-d) Thermal images recorded at 30, 60 and 180 seconds of laser irradiation, respectively. All images cover a 20 mm by 20 mm region.

The cylindrical inclusion representing the tumor is easily identified in the grayscale B-mode ultrasound image (Fig. 4(a)). Data obtained from the water bath experiments (Fig. 3(a)) was used to convert the normalized time shifts from the captured ultrasound frames to temperature. The thermal maps (Figs. 4(b-d)) after 30, 60 and 180 seconds show the progressive increase in temperature. At 180 seconds, the target inclusion reached a temperature increase of over 7°C while the surrounding material had a temperature rise of less than 2°C . In these images, temperature increase was confined to the inclusion due to the presence of embedded photoabsorbers. Since thermal images are obtained from ultrasound images, both types of images are spatially co-registered.

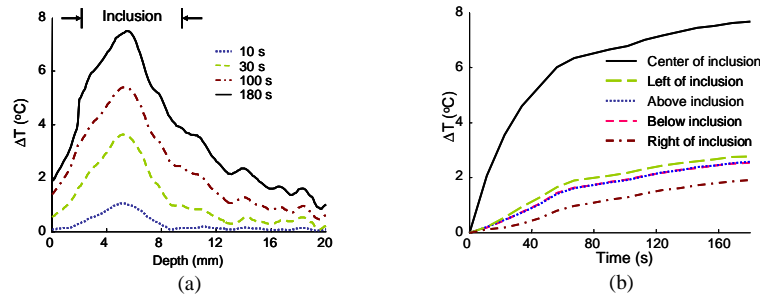


Fig. 5. (a) Spatial temperature profile along the axial line passing through the center of the inclusion. (b) Temporal temperature profile measured inside the inclusion and four regions outside of the inclusion located 6 mm to the left, above, below and to the right from the center of the inclusion having 3.5 mm radius.

Figure 5 presents further spatio-temporal examination of the temperature rise. Spatial profile of temperature distribution along the vertical line passing through the center of the inclusion shows that the temperature rise is primarily localized to the area with embedded photoabsorbers (Fig. 5(a)). After 180 seconds of therapy, the temperature increased from a baseline (room temperature) by more than 7°C . In addition, time-dependent temperature rise was examined in a 1 mm by 1 mm region inside the inclusion and four regions located 6 mm to the right, to the left, above and below from the center of the 3.5-mm radius inclusion (Fig. 5(b)). Mean temperature in the inclusion increases monotonically with time. Rate of temperature rise in the inclusion is nonlinear due to heat diffusion into surrounding material. Temperature in the background regions surrounding the inclusion also increases with time (Fig. 5(b)) due to both heat diffusion from the inclusion and heat generated by the small absorption of radiant energy. Therefore, the region closest to the laser irradiation side (located to the left from the inclusion) has the highest temperature rise while the region behind the inclusion (located to the right) being furthest away from the laser irradiation spot has the lowest rise in temperature. Finally, the regions above and below the inclusion, being equidistant from the laser irradiation site and the target inclusion, have similar temperature rise.

4.2. Ex-vivo tissue studies

Temperature monitoring during laser irradiation was also performed on fresh porcine muscle tissue. The ultrasound and thermal images (20 mm by 15 mm field of view) are presented in Figs. 6(a-e). The site of laser irradiation and nanoparticle injection are indicated in the ultrasound image (Fig. 6(a)). After 20 seconds of photothermal therapy, the temperature increased by 3°C, 6°C and 8°C for laser irradiances of 2, 3 and 4 W/cm² respectively (Figs. 6(c-e)). As expected, higher energies lead to a greater temperature increase. The heated region was located 8 mm from the surface of the tissue where the photoabsorbers were injected. Negligible temperature increase was observed in the control tissue (tissue sample injected with water) after 120 seconds of therapy (Fig. 6(b)).

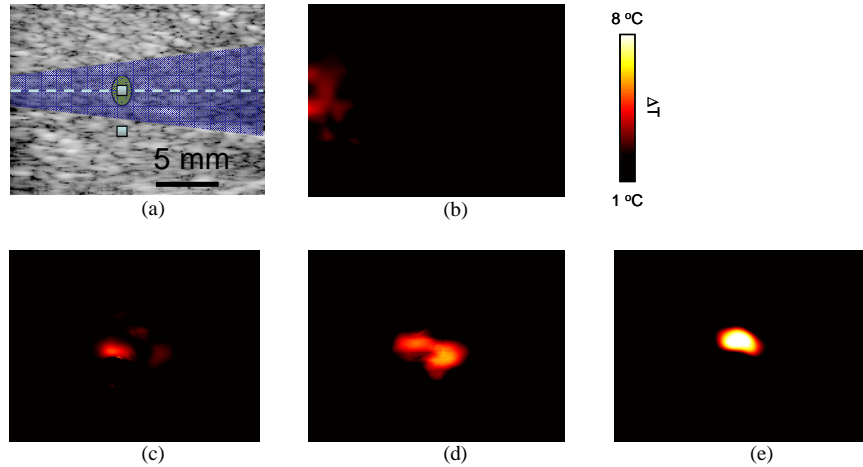


Fig. 6. (a) Ultrasound image of the porcine tissue sample where the photoabsorber injection site with respect to the laser beam is indicated by the circle. (b) The thermal image of the tissue sample injected with water and irradiated for 120 seconds at 2 W/cm² indicates negligible laser heating of the specimen. In contrast, thermal images (c-e) of the tissue injected with photoabsorbers and irradiated for 20 seconds at 2, 3 and 4 W/cm² respectively, clearly indicate progressive and localized temperature increase. All images cover a 20 mm by 15 mm region.

Spatial temperature profiles (Fig. 7(a)) were computed along the direction of laser beam, i.e., the horizontal line shown in Fig. 6(a). Two tissue samples (one sample containing injected nanoparticles and another control sample injected with water without nanoparticles) underwent laser heating for 120 seconds at 2 W/cm². In both samples, the temperature rises by about 4°C near the surface and then rapidly falls to below 1°C at a depth of 3 mm. However in the tissue with nanoparticles, the temperature rise exceeds 12°C at a depth of 8 mm. This thermal zone is highly localized and corresponds to the targeted site with injected photoabsorbers. In the control tissue sample, no significant temperature rise was observed beyond 3 mm from the tissue surface. The temporal behavior of temperature (Fig. 7(b)), measured within a 1.5 mm by 1.5 mm region inside and outside the targeted site was similar to that observed in the phantom experiment. In the targeted area, a steady increase in average temperature with time reached over 10°C after 120 seconds of laser irradiation while the temperature in the background tissue (outside of the targeted area) showed a gradual, 1.5°C temperature increase due to thermal diffusion and negligible optical absorption.

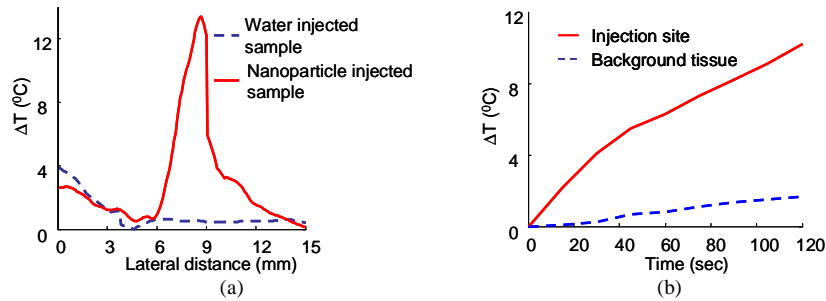


Fig. 7. (a) Spatial temperature profile measured along the horizontal dotted line shown in Fig. 6(a) for tissue specimens injected with either aqueous solution of photoabsorbers and water without photoabsorbers. (b) Temporal temperature profile measured inside and outside of the targeted area (site of injection). The 1.5 mm by 1.5 mm regions for temporal assessment of temperature are indicated by squares in Fig. 6(a).

Ultrasound images recorded before and after irradiation (Figs. 8(a-b)), covering 16 mm by 12 mm field of view, demonstrate the spatial location and extent of the thermal lesion created during laser heating. The experiment was performed on a tissue sample irradiated at 3 W/cm² for 180 seconds. The thermal map (Fig. 8(c)) shows that the temperature increased by over 25°C in the targeted region with injected photoabsorbers. In ultrasound images, there was an increase in echogenicity at the injection site after laser irradiation accompanied by a shadow below the region of high echogenicity (Fig. 8(b)). Per ultrasound and thermal images, the rounded, 3 mm diameter heated region is located at 8 mm depth. Visual inspection of the sample cross-section (Fig. 8(d)) reveals that the location of the injection site is consistent with the region of elevated temperature observed in both ultrasound and thermal images.

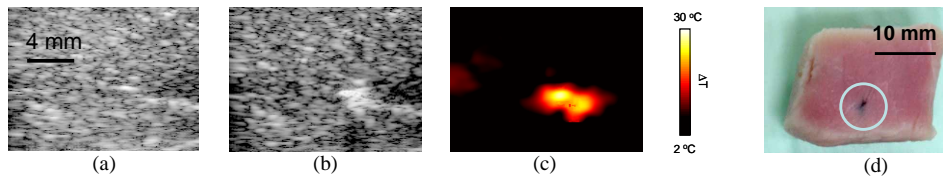


Fig. 8. Photothermal laser heating of porcine muscle tissue (16 mm by 12 mm) performed using 3 W/cm² laser irradiation for 180 seconds. Ultrasound image (a) before and (b) after laser irradiation indicate the location of heated region associated with changes in echogenicity. The location and the extend of the heated region is further confirmed in (c) thermal image computed after 180 seconds of laser heating. The region of elevated temperature is consistent with injection site visible on the photograph (d) of the tissue sample.

5. Discussion

The 532 nm optical wavelength used in this study closely matches the absorption spectra of the photoabsorbers. However, to carry out photothermal therapy at reasonable depths, laser irradiance in the near infrared (NIR) spectrum must be used [23]. In addition, various photoabsorbers such as gold nanorods, nanoshells, and nanocrescents have their optical absorption resonance in this NIR window [3-5]. By selecting a wavelength in the NIR and appropriately matched photoabsorbers, tumors at depths of a few centimeters can be treated photothermally.

The temperature distribution during photothermal therapy is affected by two processes – heat generation due to absorption of laser energy and spatial redistribution of heat due to thermal diffusion. Mean temperature in the tumor-mimicking inclusion with embedded nanoparticles increases with laser heating over time (Figs. 5(b) and 7(b)). Heat diffusion results in a gradual increase of temperature around the therapeutic zone. Therefore, during the photothermal therapy, it is essential to monitor temperature not only within the tumor, but also

in the surrounding healthy tissues. Ultrasound and thermal images (Figs. 4 and 8) illustrate the feasibility of spatial and temporal tracking of temperature increase throughout the region of interest. Thermal maps show a progressive temperature increase in tissue under laser irradiation. The heated zone was shown to be highly localized to the photoabsorber embedded region. The results indicate that ultrasound-based imaging is a candidate approach to guide and monitor photothermal cancer therapy.

In the preliminary experiments performed here, the laser irradiation was delivered from the left side of the specimen (Fig. 2). In clinical settings, a more practical configuration is preferable with light delivery and acoustic transducer on the same side. For example, optical fibers placed along the sides of the transducer can be used for delivering the radiant energy to the tissue [24-26].

A pre-therapy calibration was performed to establish the relationship between normalized time shift and temperature. However, it is possible to measure temperature using a generalized and known *a priori* tissue specific calibration [11]. A database can be obtained to allow calculation of temperature from ultrasound time shifts directly without a calibration procedure. For tissue temperatures of 55°C and higher, the backscattered ultrasound signal will be significantly different due to tissue state change [27]. Under such circumstances, the ultrasound-based estimation of temperature may fail to provide accurate results. However, breakdown of ultrasound temperature monitoring may also suggest thermal damage and possibly confirm the success of treatment.

Physiological motion (e.g., cardiac, respiratory) could lead to artifacts in ultrasound based temperature measurements. For example, periodic heart beats cause tissue motion which appears as time shifts on the ultrasound signal and could lead to an error in the temperature measurement. However, utilizing an electrocardiogram (ECG) to trigger data capture, ultrasound frames can be collected at the same point in the cardiac cycle and thus potentially minimize motion artifacts [28].

Finally, ultrasound can be combined with photoacoustic and elasticity imaging to form a synergistic imaging system [29]. The same transducer can be used in ultrasound, photoacoustic and elasticity imaging [29]. The imaging contrast in photoacoustic imaging is provided by the inherent difference in the optical properties of the tumor and surrounding tissue [30]. Photoabsorbers used during photothermal therapy significantly enhance this optical contrast [31]. Therefore, photoacoustic imaging can be used to visualize the tumor and identify the presence of photoabsorbers. Elasticity imaging on the other hand employs the difference in tissue stiffness for image contrast. Elastic properties of thermally damaged and cancerous tissue are vastly different from normal tissue [32]. Progression of tumor necrosis can be assessed using elasticity imaging at regular intervals during and after therapy [13, 32]. Ultrasound, photoacoustic and elasticity imaging can be utilized to evaluate anatomical, functional and mechanical properties of tissue during therapy, thus providing additional diagnostic tools to the clinician.

6. Conclusions

Results of this study suggest that ultrasound can be used to non-invasively image and guide photothermal cancer therapy. Experimental results show that temperature elevations of more than 20°C can be obtained using gold nanocolloids and matching continuous wave laser irradiation. Furthermore, the temperature increase during the photothermal therapy can be monitored by ultrasound-based thermal imaging. Changes in ultrasound and thermal images were consistent with visual inspection of the tissue samples after laser heating experiments.

Acknowledgements

The authors would like to thank Mr. Larson for his help in preparing the gold nanoparticles, and Dr. Dunn and Mr. Estrada for providing access to the continuous wave laser.